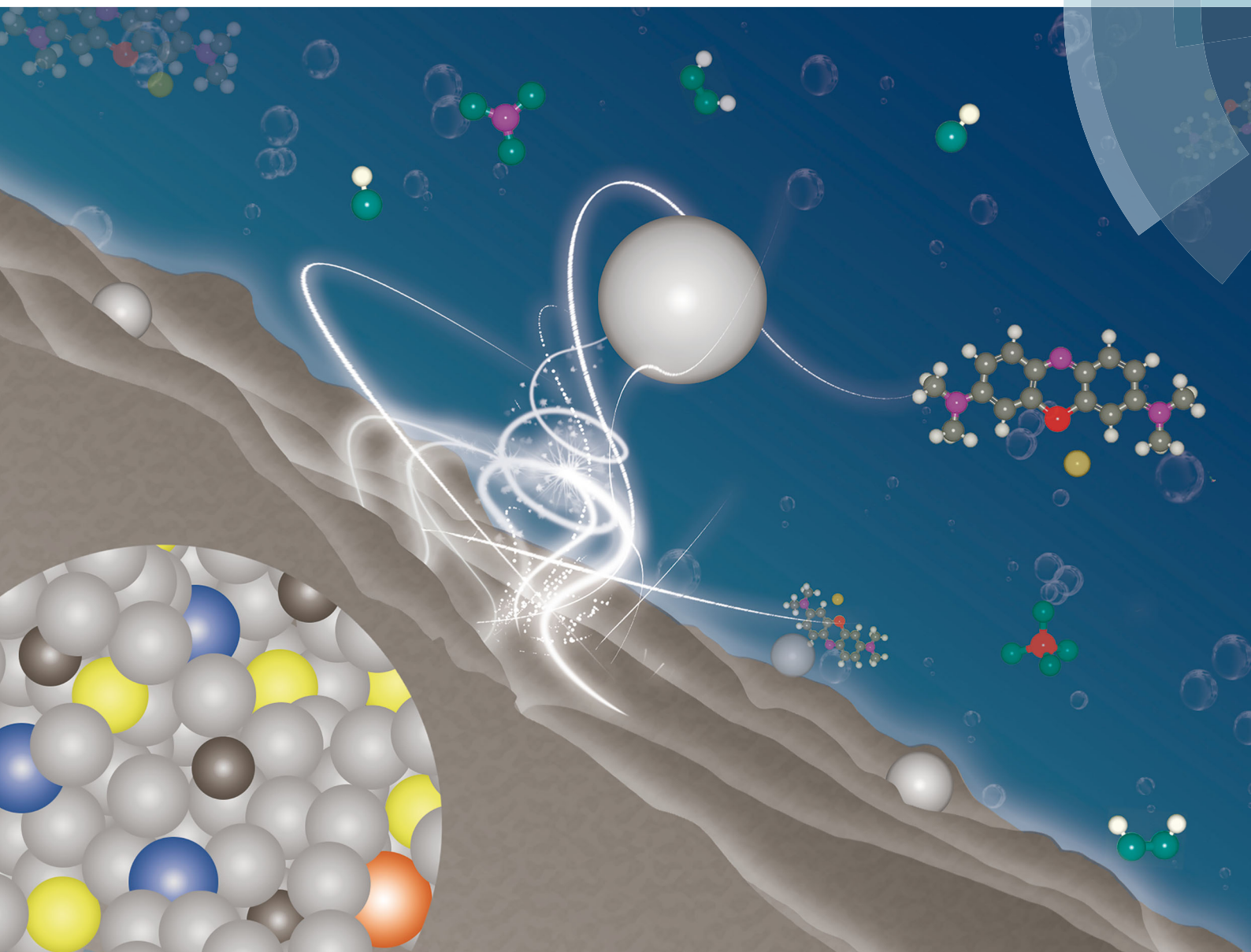


# NJC

New Journal of Chemistry  
rsc.li/njc

A journal for new directions in chemistry



ISSN 1144-0546



ROYAL SOCIETY  
OF CHEMISTRY

Celebrating  
IYPT 2019

PAPER


Baolong Shen *et al.*  
Effect of Co addition on catalytic activity of FePCCu  
amorphous alloy for methylene blue degradation





Cite this: *New J. Chem.*, 2019, **43**, 6126

# Effect of Co addition on catalytic activity of FePCCu amorphous alloy for methylene blue degradation†

Long Hou,<sup>a</sup> Qianqian Wang,<sup>a</sup> Xingdu Fan,<sup>a</sup> Fang Miao,<sup>a</sup> Weiming Yang<sup>b</sup> and Baolong Shen  <sup>\*,ab</sup>

The effect of Co addition on the decolorization performance of the FePCCu amorphous alloy for degrading methylene blue (MB) is investigated. It is found that 100 mg L<sup>-1</sup> MB solution can be rapidly degraded within 9 min via 0.5 g L<sup>-1</sup> FeCoPCCu ribbon dosage and 1 mM H<sub>2</sub>O<sub>2</sub> at 298 K at pH = 3. The amorphous state induced by the Co addition, nano-whisker and micro-crack structures formed during the decolorization process and local galvanic couples between bonds of metal–metalloid elements accelerate the electron and mass transfer of FeCoPCCu amorphous ribbons and result in their good catalytic ability. The catalytic performance of alloys with different Co additions is highly related to their corrosion resistance. Good environmental applicability and reusability of the alloys are also explored. The present work reveals that appropriate Co addition has a significant influence on the catalytic activity of Fe-based amorphous alloys, and this alloy is proposed as a new catalyst for sewage treatment.

Received 23rd January 2019,  
Accepted 17th March 2019

DOI: 10.1039/c9nj00369j

rsc.li/njc

## Introduction

Synthetic dyes, which are indispensable in the textile industry, have caused serious environmental problems. Zero-valent iron (ZVI) has been widely used in decomposing hazardous organics in wastewater, including synthetic dyes, phenols, *etc.*, due to its good environmental compatibility, abundant sources and non-toxic by-products.<sup>1–3</sup> In the past several decades, in order to improve the chemical reactivity of ZVI, some new materials including nano-ZVI, Pd/Fe bimetallic alloys, and nano-ZVI and activated carbon composites have been successfully proposed.<sup>4–7</sup> Specifically, by ball-milling a rapidly solidified cast iron ribbon, ZVI powders with a highly efficient degradation ability for ethyl-orange and direct blue-6 were prepared.<sup>8</sup> However, there is an inevitable fact that ZVI can be easily oxidized, which causes a dense oxidation product coating on ZVI and greatly impedes its degradation ability. Therefore, it is urgent to optimize the degradation performance of ZVI in dye solution from a new perspective.

Fe-based amorphous alloys, as metastable materials, have a combination of unique mechanical, magnetic and chemical

properties,<sup>9–12</sup> and are considered as promising materials for industrial applications. In particular, their good catalytic properties have been highlighted due to the far-from-equilibrium structures and high-energy states of the amorphous alloys,<sup>13</sup> which may support more reactive sites than those of traditional crystalline ZVI during the degradation process. Therefore, Fe-based amorphous alloys are expected to have wide application prospects as catalysts in wastewater treatment.

Recently, there has been some research about the degradation of hazardous organics using Fe-based amorphous alloys. Tang *et al.* reported that the Fe–B binary amorphous alloy exhibited a higher degradation efficiency than its crystalline counterpart and traditional iron powders, and the high reaction activity was closely related to the low activation energy (25.43 kJ mol<sup>-1</sup>) of the degradation reaction using the FeB amorphous alloy.<sup>14</sup> Addition of metalloid Si into the FeB amorphous alloy could form a non-compact oxide layer which could easily fall off, ensuring the continuous contact of the dye solution with the ribbon surface.<sup>15,16</sup> Moreover, Wang *et al.* proposed that the large specific surface area of the ball-milled FeNbSiB amorphous powder largely improved its degradation performance.<sup>17</sup> Minor Y additions in FeSiB metallic glass powders lead to the formation of local galvanic cells between Fe-rich and Fe-poor atomic clusters to accelerate electron transfer and promote rapid degradation of dyes.<sup>18</sup>

More recently, our group found that the FePC amorphous alloy had a higher decolorization efficiency than the FeSiB amorphous alloy in wastewater remediation due to the structural

<sup>a</sup> Jiangsu Key Laboratory of Advanced Metallic Materials, School of Materials Science and Engineering, Southeast University, Nanjing 211189, China.  
E-mail: blshen@seu.edu.cn

<sup>b</sup> Institute of Massive Amorphous Metal Science, China University of Mining and Technology, Xuzhou 221116, China

† Electronic supplementary information (ESI) available. See DOI: 10.1039/c9nj00369j

heterogeneity between the strong Fe–C and weak Fe–P bonds,<sup>19</sup> which can accelerate the electron transfer from ZVI. With Cu addition, the FePCCu alloy should have a higher degree of structural heterogeneity due to the positive enthalpy of mixing (+13 kJ mol<sup>−1</sup>) between Fe and Cu,<sup>20</sup> and thus, it may have an excellent degradation ability in wastewater treatment. However, no investigation has been made on the degradation ability of FePCCu amorphous alloys to date. Furthermore, ball-milled CoSiB powder showed several thousand times higher degradation ability than ZVI,<sup>21</sup> while amorphous CoSiB ribbons can only adsorb dye molecules instead of decomposing them (Zhang *et al.*, 2018).<sup>22</sup> The effect of Co on the decolorization process of dye molecules is controversial and needs further investigation.

In this work, the effect of Co addition on the catalytic performance of degrading MB using FePCCu ribbons *via* Fenton-like reactions is investigated in detail. The environmental applicability and reusability of Fe(Co)PCCu amorphous ribbons are also discussed.

## Experimental

### Sample and reagent preparation

Multi-component alloy ingots with nominal compositions of Fe<sub>83.2−x</sub>Co<sub>x</sub>P<sub>10</sub>C<sub>6</sub>Cu<sub>0.8</sub> ( $x = 0, 4$  and  $10$  at%, denoted as Co<sub>0</sub>, Co<sub>4</sub> and Co<sub>10</sub>, respectively) were prepared by induction-melting mixtures of pure Fe (99.99 wt%), Cu (99.995 wt%), Co (99.99 wt%), pre-alloyed Fe–P ingots (consisting of 75 wt% Fe and 25 wt% P) and Fe–C ingots (consisting of 96 wt% Fe and 4 wt% C) in an induction melting furnace under a purified argon atmosphere (99.999%). The master alloy ingot was re-melted in a special quartz tube at a pressure of  $5 \times 10^{-3}$  Pa in a furnace chamber and then sprayed rapidly onto the surface of a high-speed rotating single roller with a pressure difference of 0.02 MPa between the furnace chamber and a special quartz tube (roller speed 40 m s<sup>−1</sup>) to form quenched (AQ) ribbons, and the width and thickness of ribbons were 1 mm and 22  $\mu$ m, respectively. Commercially available methylene blue (MB, C<sub>16</sub>H<sub>18</sub>ClN<sub>3</sub>S, AR grade), hydrogen peroxide (H<sub>2</sub>O<sub>2</sub>, AR grade), sulphuric acid (H<sub>2</sub>SO<sub>4</sub>, AR grade) and sodium hydroxide (NaOH, AR grade) were purchased from Xiya Reagent, Sinopharm Chemical Reagent Co., Ltd, Chron Chemicals and Greagent, respectively.

### Characterization

The microstructure of the ribbons was characterized by X-ray diffraction (XRD, Bruker D8 Discover) with Cu K $\alpha_1$  radiation and transmission electron microscopy (TEM, FEI Tecnai G2 F20). Thermal parameters were measured by using a differential scanning calorimeter (DSC, NETZSCH 404 F3) under a flow of high purity argon at a heating rate of 0.67 K s<sup>−1</sup>. The samples for TEM analyses were thinned carefully by a low-angle (10°) ion milling system (Gatan Inc., PIPS-M691) at 5 kV under liquid nitrogen cooling from both sides of the ribbons. After perforation, the ribbons were further thinned by a lower-angle (4°) ion milling system at 4 kV under the same condition for  $\sim 10$  min to obtain an  $\sim 100$  nm thin zone. The surface morphology and

elemental composition of the AQ and reacted ribbons were studied using a scanning electron microscope (SEM, FEI Sirion 200) using an energy dispersive spectrometer (EDS).

### Chemical tests

For all chemical tests, solutions were prepared using deionized (DI) water in a 500 mL beaker, and the temperature, pH, MB concentration ( $C_{\text{MB}}$ ), H<sub>2</sub>O<sub>2</sub> concentration ( $C_{\text{H}_2\text{O}_2}$ ) and ribbon dosage of the degradation experiments were set according to specific experimental requirements. The prepared solution with ribbons (ribbons were cut into 1 cm long strips) was stirred continuously at a constant rate using a mechanical stirrer during the degradation process. The real-time concentration of the MB solution was monitored using a UV-vis spectrophotometer (Shimadzu UV-1280). The electrochemical properties including polarization curves and electrochemical impedance spectroscopy (EIS) were measured using an electrochemical measuring instrument (Gamry Interface 1000) in 0.5 mol L<sup>−1</sup> NaCl solution at ambient temperature. The tests were performed using a three-electrode method, *i.e.* working electrode (sample), reference electrode (Ag/AgCl electrode), and opposition electrode (Pt electrode). The samples were immersed in an electrolyte for 10–60 min, and the open-circuit potential ( $E_{\text{OCP}}$ ) was considered to be stable when the variation was within the range of  $\pm 5$  mV. The dynamically polarized processes were recorded at  $-250$  mV from  $E_{\text{OCP}}$  at a voltage scanning rate of 4 mV s<sup>−1</sup>, and the scanning frequencies of EIS were from 100 kHz to 0.01 Hz. It is worth noting that as the ribbons for electrochemical tests were immersed in the solution without encapsulation, both sides of the ribbons were considered for current density normalization. The length of the immersed ribbons was 1 cm. Besides, the side surfaces are much smaller than the top and bottom surfaces. Thus, the effective surface area of the electrode was 0.2 cm<sup>2</sup>.

## Results

### Microstructure

Fig. 1(a) shows the XRD patterns of the air side of the AQ Co<sub>0</sub>, Co<sub>4</sub> and Co<sub>10</sub> ribbons. The XRD curve of the Co-free alloy shows a small crystallization peak at  $2\theta = 45^\circ$  which is related to the (110)-reflection of the  $\alpha$ -Fe crystalline phase, indicating the poor amorphous forming ability of the alloy. For alloys with Co addition, only a diffuse diffraction characteristic without any detectable sharp peak was observed, suggesting an amorphous feature. The microstructures of the Co<sub>0</sub>, Co<sub>4</sub> and Co<sub>10</sub> samples were further characterized using TEM with results shown in Fig. 1(b), (c) and (d), respectively. A small quantity of nanocrystals can be observed for the Co<sub>0</sub> alloy, and the SAED pattern in the inset of Fig. 1(b) confirms that the crystals are  $\alpha$ -Fe. In contrast, for the Co<sub>4</sub> and Co<sub>10</sub> alloys, no crystalline phase appears in their TEM images. The SAED patterns of the Co-added alloys consist of a single diffraction halo without sharp diffraction rings, which is well consistent with the XRD measurements. The XRD and TEM results confirm that Co



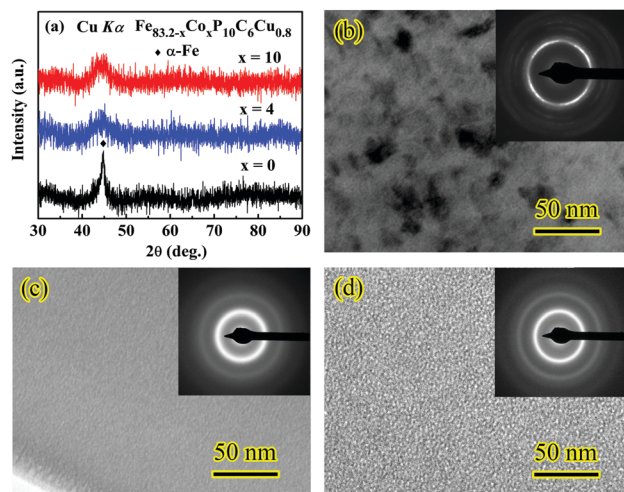


Fig. 1 (a) XRD patterns of the AQ Co<sub>0</sub>, Co<sub>4</sub> and Co<sub>10</sub> ribbons. TEM images of the Fe<sub>83.2-x</sub>Co<sub>x</sub>P<sub>10</sub>C<sub>6</sub>Cu<sub>0.8</sub> alloys: (b) Co<sub>0</sub>, (c) Co<sub>4</sub>, (d) Co<sub>10</sub>. The insets are corresponding SAED patterns.

addition can result in a fully amorphous structure in the FePCCu alloy system.

### Thermal stability

Fig. 2 shows the DSC heating curves of the AQ Co<sub>0</sub>, Co<sub>4</sub> and Co<sub>10</sub> ribbons. As Fe-based amorphous alloys with a high Fe content (>79 at%) usually have a weak amorphous-forming ability, their glass transition phenomenon is difficult to observe from DSC analyses.<sup>23</sup> As a result, the glass transition temperatures ( $T_g$ ) of the Fe<sub>83.2-x</sub>Co<sub>x</sub>P<sub>10</sub>C<sub>6</sub>Cu<sub>0.8</sub> alloys synthesized in the current work are not found on the DSC curves. However, it can be clearly seen that there are two exothermic events of alloys during heating, indicating that the crystallization of these alloys is a two-stage process. As reported by our previous work, the first exothermic peak corresponds to the precipitation of the  $\alpha$ -Fe phase while the second one corresponds to that of the Fe<sub>3</sub>P and Fe<sub>3</sub>C compounds.<sup>24</sup> With 4 at% Co addition, the onset

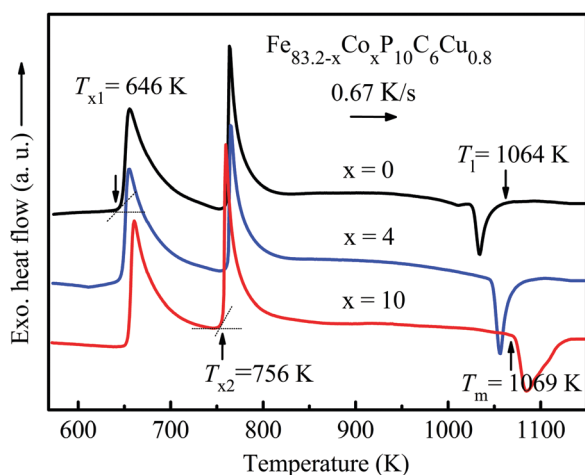


Fig. 2 DSC curves of the AQ Co<sub>0</sub>, Co<sub>4</sub> and Co<sub>10</sub> ribbons at a heating rate of 0.67 K s<sup>-1</sup>.

temperature of the first crystallization ( $T_{x1}$ ) has almost no change compared with that for the Co<sub>0</sub> alloy, while it increases slightly with further increase in Co to 10 at%, suggesting the improvement of thermal stability of the amorphous alloy with Co addition. Meanwhile, the second crystallization temperature ( $T_{x2}$ ) increases slightly for the Co<sub>4</sub> alloy and then decreases with further increase of Co to 10 at%. Accordingly, the temperature interval ( $\Delta T_x = T_{x2} - T_{x1}$ ) is first slightly increased to 116 K and then decreased to 103 K. The large  $\Delta T_x$  with a minor Co substitution also indicates the increment of thermal stability of the residual amorphous phase. Moreover, the melting temperature ( $T_m$ ) and liquid temperature ( $T_l$ ) of the alloys all move to a high temperature level with Co addition, which also indicates the improvement of thermal stability.

### Decolorization performance

To investigate the dye decolorization ability of the synthesized alloys in this work, Fenton-like reactions using AQ Co<sub>0</sub>, Co<sub>4</sub> and Co<sub>10</sub> ribbons were performed on the MB solution (reaction conditions:  $T = 298$  K,  $C_{MB} = 100$  mg L<sup>-1</sup>,  $C_{H_2O_2} = 1$  mM, ribbon dosage = 0.5 g L<sup>-1</sup>, and pH = 3). Fig. 3(a) shows the color change of the MB solution at different reaction times during the degradation process. The solution is almost colourless after 9 min using the Co<sub>4</sub> ribbons, while those using the Co<sub>0</sub> and Co<sub>10</sub> ribbons need a longer time to achieve the same result. The UV-vis absorbance spectra of the MB solutions reacting with the AQ Co<sub>0</sub>, Co<sub>4</sub> and Co<sub>10</sub> ribbons for different periods of time are shown in Fig. 3(b), (c) and (d), respectively. Four absorption peaks are detected for the MB solutions at 247 nm, 292 nm, 610 nm and 653 nm in the spectra, and the intensity of all absorption peaks decreases significantly with the reaction time, suggesting a decrease of  $C_{MB}$ . Because the peak value at 653 nm represents chromogenic species,<sup>25</sup> to understand the degradation process, the time dependences of the normalized concentration according to the absorption intensity at 653 nm in Fig. 3(b)–(d) are summarized in Fig. 3(e), with the results compared with the reactions using FePC and FeSiB from the literature.<sup>19</sup> The Co<sub>0</sub> and Co<sub>10</sub> ribbons required 15 min to degrade MB to less than 5%. For the Co<sub>4</sub> alloy, the  $C_t/C_0$  shows a more rapid descent process within 6 min, and  $C_{MB}$  is reduced to less than 5% within 9 min, which is even better than that of the FeSiB amorphous ribbon, and similar to that of the FePC amorphous ribbon. Moreover, it is found that all the degradation processes of the MB solution using Fenton-like reactions in this work follow the pseudo-first-order kinetic model:<sup>26</sup>

$$C_t = C_0 \exp(-kt) \quad (1)$$

where  $k$  is the reaction rate constant,  $t$  is the reaction time,  $C_0$  is the initial concentration of MB, and  $C_t$  is the instant concentration of MB at time  $t$ . Thus,  $k$  can be expressed as follows:

$$k = \ln \frac{C_0}{C_t} / t \quad (2)$$

According to eqn (2), Fig. 3(f) shows the change of  $\ln(C_0/C_t)$  with reaction time. The  $k$  of the Co<sub>4</sub> ribbon is 0.470 min<sup>-1</sup>, which is larger than 0.340, 0.230, 0.330 and 0.085 min<sup>-1</sup>



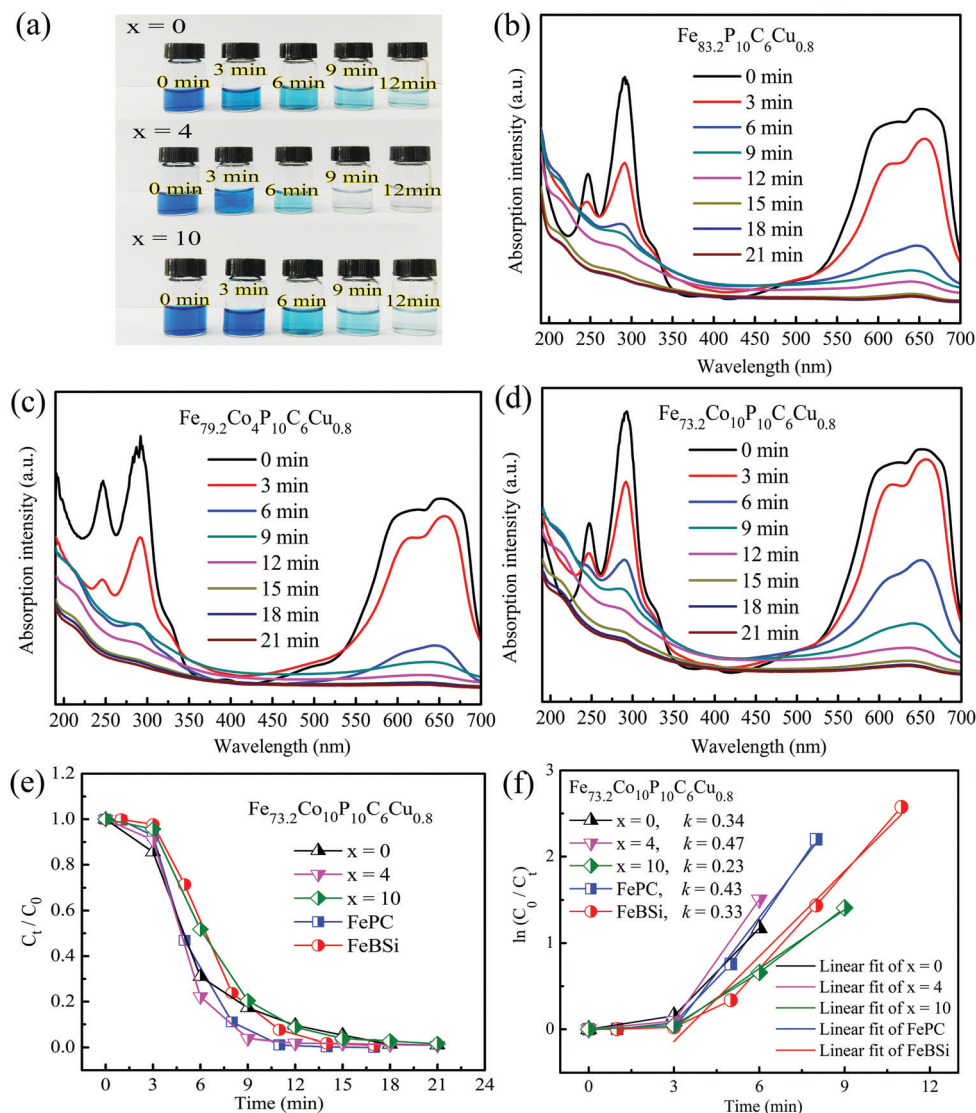


**Fig. 3** (a) Color changes of the MB solution at different times during the degradation process using the AQ Co<sub>0</sub>, Co<sub>4</sub> and Co<sub>10</sub> ribbons. The UV-vis absorbance spectra of the MB solutions during the Fenton-like reactions using ribbons: (b) Co<sub>0</sub>, (c) Co<sub>4</sub> and (d) Co<sub>10</sub>; (e) the  $C_t/C_0$  change of the MB solutions with the reaction time and (f) the change of  $\ln(C_0/C_t)$  with the reaction time for different ribbons.

for the Co<sub>0</sub>, Co<sub>10</sub>, Fe<sub>78</sub>Si<sub>9</sub>B<sub>13</sub> and Fe<sub>73.5</sub>Si<sub>13.5</sub>B<sub>9</sub>Cu<sub>1</sub>Nb<sub>3</sub><sup>27</sup> ribbons, respectively, and slightly higher than 0.430 min<sup>-1</sup> for the Fe<sub>80</sub>P<sub>13</sub>C<sub>7</sub> ribbons. The details can be seen in Table 1. This is consistent with the visualized decolorization phenomenon in Fig. 3(a), suggesting a fast degradation process in the MB solution using the Co<sub>4</sub> ribbons. It is worth noting that after degradation, some by-products in the reaction

solution were observed. To identify these, FTIR and Raman analyses of the by-product powders were carried out. The details of the experimental processes are shown in the supplementary file, and the results are shown in Fig. S1 and S2 (ESI<sup>†</sup>). All these results clearly indicate the decomposition of MB and oxidation of zero-valent iron during the Fenton-like reaction.

**Table 1** Degradation characterizations of the Fe<sub>83.2-x</sub>Co<sub>x</sub>P<sub>10</sub>C<sub>6</sub>Cu<sub>0.8</sub>, Fe<sub>78</sub>Si<sub>9</sub>B<sub>13</sub>, Fe<sub>80</sub>P<sub>13</sub>C<sub>7</sub> and Fe<sub>73.5</sub>Si<sub>13.5</sub>B<sub>9</sub>Cu<sub>1</sub>Nb<sub>3</sub> amorphous alloys

Alloys	pH	Solution concentration (mg L <sup>-1</sup> )	Ribbon dosage (g L <sup>-1</sup> )	Degradation rate constant $k$ (min <sup>-1</sup> )	Reaction type
Fe <sub>83.2</sub> P <sub>10</sub> C <sub>6</sub> Cu <sub>0.8</sub>	3	100	0.5	0.340	Fenton-like
Fe <sub>79.2</sub> Co <sub>4</sub> P <sub>10</sub> C <sub>6</sub> Cu <sub>0.8</sub>	3	100	0.5	0.470	Fenton-like
Fe <sub>73.2</sub> Co <sub>10</sub> P <sub>10</sub> C <sub>6</sub> Cu <sub>0.8</sub>	3	100	0.5	0.230	Fenton-like
Fe <sub>78</sub> Si <sub>9</sub> B <sub>13</sub> <sup>19</sup>	3	100	0.5	0.330	Fenton-like
Fe <sub>80</sub> P <sub>13</sub> C <sub>7</sub> <sup>19</sup>	3	100	0.5	0.430	Fenton-like
Fe <sub>73.5</sub> Si <sub>13.5</sub> B <sub>9</sub> Cu <sub>1</sub> Nb <sub>3</sub> <sup>27</sup>	2.8	238	0.5	0.085	Fenton-like

### Surface morphology

Since the degradation process is a surface-mediated catalytic reaction and different surfaces may cause different degradabilities,<sup>28</sup> the surface morphology of the FePCCu ribbon with different Co contents before and after the decolorization reaction were analyzed using SEM as shown in Fig. 4. For the three kinds of AQ ribbons before the reaction, typically smooth surfaces without apparent defects were observed as shown in Fig. 4 (a, Co<sub>0</sub>), (c, Co<sub>4</sub>) and (e, Co<sub>10</sub>), respectively, and the results of EDS in Table 2 reveal

the normal compositions of all the alloys. A large number of corrosive pits are formed with sizes of about 2–4 μm on the surface of the reacted Co<sub>0</sub> ribbon (Fig. 4(b)), indicating that corrosion occurred during the degradation process. To further confirm the extent of corrosion, an enlarged pit center is evaluated using EDS with results in the inset of Fig. 4(b). As the content of carbon cannot be accurately measured with EDS, the composition analysis *via* EDS was carried out without measuring the carbon content in this work. A higher content

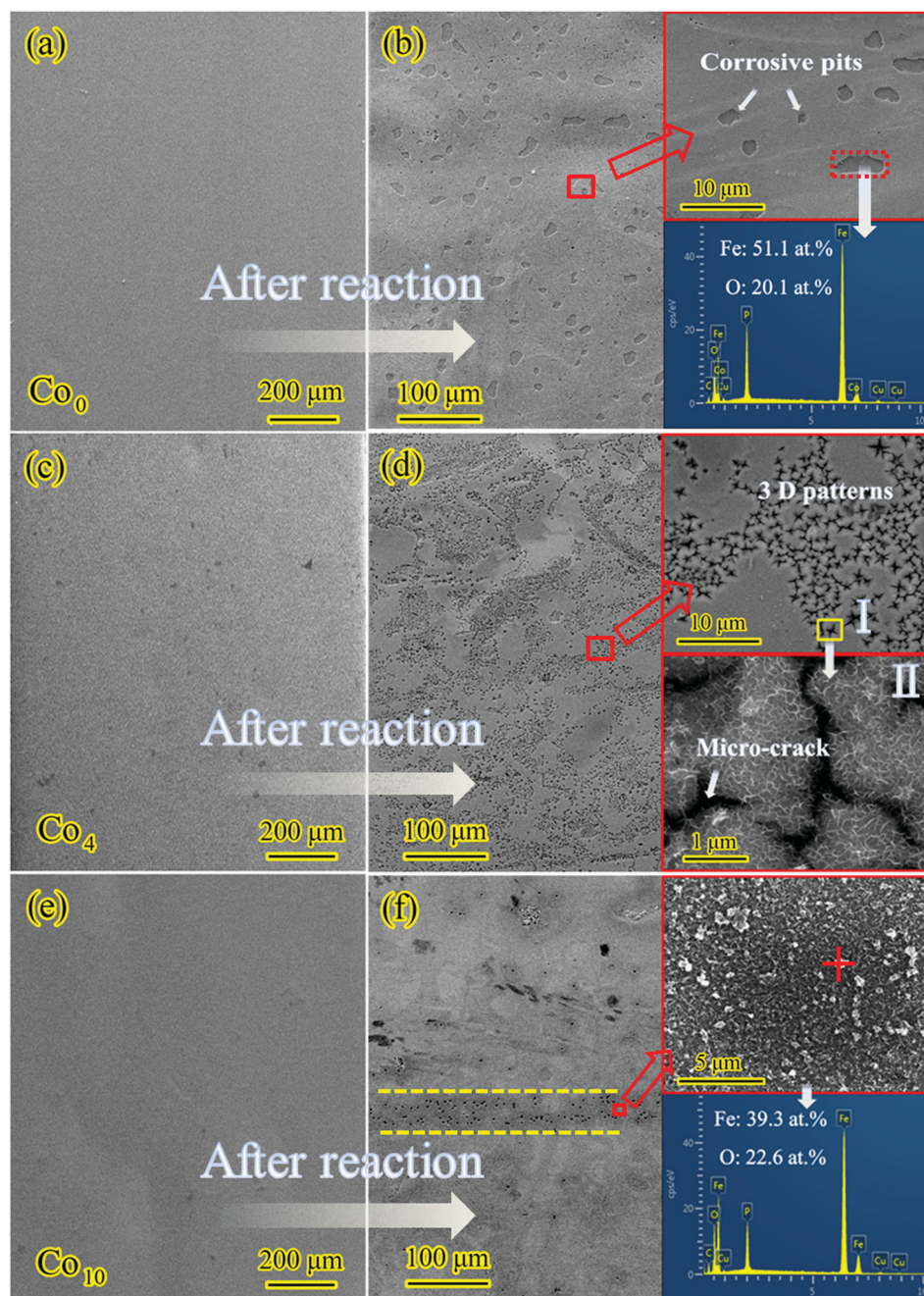


Fig. 4 SEM images of the AQ ribbons before the reaction: (a) Co<sub>0</sub>, (c) Co<sub>4</sub>, and (e) Co<sub>10</sub>. SEM images of the AQ ribbons after the reaction: (b) Co<sub>0</sub>, (d) Co<sub>4</sub>, and (f) Co<sub>10</sub>. The inset of (b) is the enlarged image and corresponds to the EDS analysis of the pitting area; the insets of (d) are the enlarged images; and the inset of (f) is the enlarged image and corresponds to the EDS mapping.



Table 2 EDS analysis of the AQ and reacted Fe(Co)PCCu ribbons (at%)

	Fe	Co	P	C	O	Cu
Fe <sub>83.2</sub> P <sub>10</sub> C <sub>6</sub> Cu <sub>0.8</sub> (AQ)	52.6	—	6.5	40.4	—	0.6
Fe <sub>83.2</sub> P <sub>10</sub> C <sub>6</sub> Cu <sub>0.8</sub> (after 1 cycle – corrosive pits)	51.1	—	11.3	16.5	20.1	1.1
Fe <sub>83.2</sub> P <sub>10</sub> C <sub>6</sub> Cu <sub>0.8</sub> (after 1 cycle – unreacted ribbon region)	57.3	—	10.8	27.9	3.1	0.9
Fe <sub>79.2</sub> Co <sub>4</sub> P <sub>10</sub> C <sub>6</sub> Cu <sub>0.8</sub> (AQ)	48.7	2.8	6.3	41.8	—	0.4
Fe <sub>79.2</sub> Co <sub>4</sub> P <sub>10</sub> C <sub>6</sub> Cu <sub>0.8</sub> (after 1 cycle)	29.4	3.8	11.5	25.3	28.9	1.1
Fe <sub>79.2</sub> Co <sub>4</sub> P <sub>10</sub> C <sub>6</sub> Cu <sub>0.8</sub> (after 12 cycle – red cross)	50.3	6.5	5.8	29.3	7.0	1.1
Fe <sub>79.2</sub> Co <sub>4</sub> P <sub>10</sub> C <sub>6</sub> Cu <sub>0.8</sub> (after 12 cycle – yellow cross)	35.2	5.3	15.5	16.0	26.6	1.4
Fe <sub>73.2</sub> Co <sub>10</sub> P <sub>10</sub> C <sub>6</sub> Cu <sub>0.8</sub> (AQ)	47.2	7.0	6.5	38.8	—	0.5
Fe <sub>73.2</sub> Co <sub>10</sub> P <sub>10</sub> C <sub>6</sub> Cu <sub>0.8</sub> (after 1 cycle – selective corrosion area)	39.3	5.5	7.2	24.3	22.6	1.1

of O (20.1 at%) and a lower content of Fe (51.1 at%) in the corrosive pit compared with the unreacted ribbon region (O: 3.1 at%, Fe: 57.3 at%) suggest the formation of oxides at the corrosion pit area. P and Cu element contents are almost unchanged (shown in Table 2). This result implies that the existence of  $\alpha$ -Fe nanocrystals for the Co<sub>0</sub> ribbon seems to provide a good dependence point for the occurrence of corrosion. The main reacted region of the Co<sub>4</sub> ribbons as shown in Fig. 4(d) exhibits the well-developed micro-crack structure, and the details are shown in the inset of Fig. 4(d). Region II is the enlarged image of region I, clearly showing that the dense nano-whisker oxidation products are separated by micro-cracks. Such a nano-whisker and micro-crack structure promotes penetration of the MB solution into the ribbon below the oxide layer and thus guarantees a sustained and rapid degradation process, which is similar to the catalytic process of the 3D hierarchical MnO<sub>2</sub> microspheres having porous structures with a high specific surface area and large pore volume.<sup>29</sup> This is a possible reason why the Co<sub>4</sub> alloy represents a high degradation rate compared with that of the Co<sub>0</sub> alloy. With excessive additions of Co, the selective corrosion area can be seen with a high oxygen content (22.6 at%) detected around it, suggesting the formation of the oxidized layer. Except for this, no obvious change on the surface of the reacted Co<sub>10</sub> ribbon was found (in Fig. 4(f) and inset), indicating a good corrosion resistance for the Co<sub>10</sub> ribbons.

### Corrosion resistance

As mentioned above, the degradation ability of amorphous ribbons is believed to be determined by the electron transfer rate, which is related to their corrosion resistance. Thus, the corrosion resistances of Fe(Co)PCCu alloys were investigated as shown in Fig. 5. Potentiodynamic polarization curves of the AQ Fe<sub>83.2-x</sub>Co<sub>x</sub>P<sub>10</sub>C<sub>6</sub>Cu<sub>0.8</sub> ribbons in 0.5 M NaCl solutions are shown in Fig. 5(a). The corrosion current density ( $I_{\text{corr}}$ ) of the Co<sub>0</sub> ribbon is  $7.851 \times 10^{-10} \text{ A cm}^{-2}$ , which is lower than  $2.398 \times 10^{-9}$  and  $3.684 \times 10^{-9} \text{ A cm}^{-2}$  for the Co<sub>4</sub> and Co<sub>10</sub> ribbons, whereas the values of corrosion potential ( $E_{\text{corr}}$ ) of the Co<sub>10</sub> ribbon shift to a more positive potential, *i.e.* showing a higher  $E_{\text{corr}}$  of  $-0.54 \text{ V}$  compared with  $-0.59$  and  $-0.57 \text{ V}$  for the Co<sub>0</sub> and Co<sub>4</sub> alloys, respectively. It is well known that the lower corrosion current density and higher corrosion potential imply the better corrosion resistance of the alloys.<sup>30,31</sup> Evaluations of the corrosion resistance from  $I_{\text{corr}}$  and  $E_{\text{corr}}$  seem to

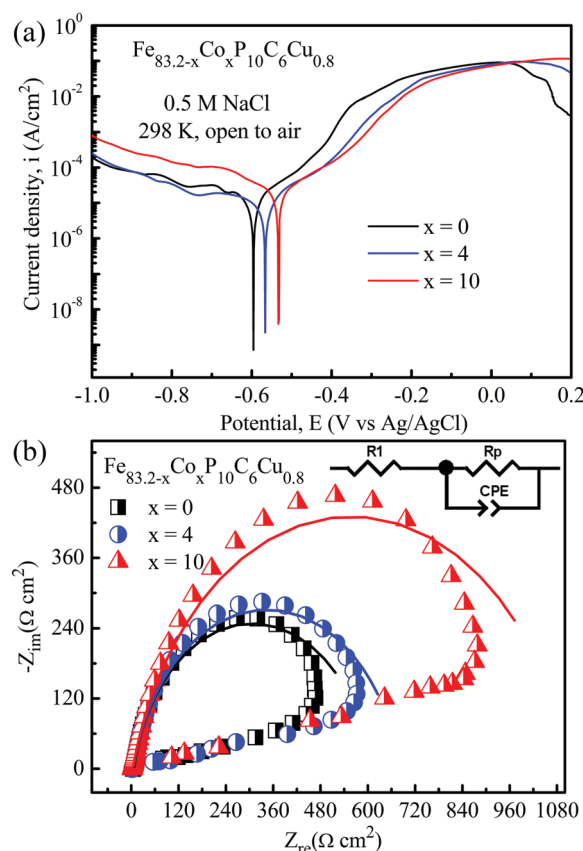


Fig. 5 Electrochemical properties of the AQ Co<sub>0</sub>, Co<sub>4</sub> and Co<sub>10</sub> ribbons in 0.5 M NaCl solutions at room temperature: (a) polarization curves and (b) Nyquist plots, and the inset corresponds to the equivalent circuit.

contradict each other. Thus, EIS was measured for the FePCCu alloys with different Co contents as shown in Fig. 5(b). Each of the Nyquist plots consists of only a single capacitance loop, suggesting that there is only one time constant for the corrosion process, which is controlled by an electrode/solution double layer. The equivalent circuit in the inset of Fig. 5(b) is used to fit the EIS data of the synthesized amorphous alloys.  $R_1$  and  $R_p$  are the solution resistance and polarization resistance, respectively; CPE is the constant phase element of the double layer capacitance.<sup>32</sup> The figure clearly shows that the Co<sub>10</sub> alloy depicts a much larger radius of the capacitance loop, suggesting a larger  $R_p$  ( $1108 \Omega \text{ cm}^2$ ) than those of the other alloys ( $600 \Omega \text{ cm}^2$  for Co<sub>0</sub> and  $677 \Omega \text{ cm}^2$  for Co<sub>4</sub>), indicating a much



better corrosion resistance. Thus, combining the results of the polarization curve and impedance spectroscopy, the Co<sub>10</sub> alloy possesses a better corrosion resistance than that of the Co<sub>0</sub> and Co<sub>4</sub> alloys, which matches the SEM image in Fig. 4(f).

### Applicability and reusability of FeCoPCCu amorphous ribbon

As Co<sub>4</sub> amorphous ribbons have the best catalytic performance, to investigate their environmental applicability, the Fenton-like reactions using AQ Co<sub>4</sub> ribbons were carried out at least twice under different reaction conditions, including pH, C<sub>H<sub>2</sub>O<sub>2</sub></sub>, ribbon dosage and C<sub>MB</sub>, to ensure credible results. The results with deviation bars are shown in Fig. 6. To investigate the effect of pH on the catalytic efficiency, other reaction parameters were kept as constants: *T* = 298 K, C<sub>MB</sub> = 100 mg L<sup>-1</sup>, C<sub>H<sub>2</sub>O<sub>2</sub></sub> = 1 mM, and ribbon dosage = 0.5 g L<sup>-1</sup>. According to Fig. 6(a), MB is only effectively degraded in strong acidic solutions (pH = 2 and 3).

The degradation process finishes within 12 and 9 min at pH = 2 and 3, respectively. When pH = 5, 95% MB is degraded after 3 hours. When pH = 7 and 9, no decolorization phenomenon is observed within 3 hours. Here, it is worth noting that the degradation rate of the MB solution during Fenton-like reactions at pH 2 is slightly lower than that at pH 3 due to the promoted hydrogen evolution reaction with excessive H<sup>+</sup> in the solution.<sup>17</sup> As a result, the Co<sub>4</sub> ribbon exhibits the best degradation ability in the MB solution at pH 3.

The initial concentration of H<sub>2</sub>O<sub>2</sub> has a large impact on the reaction efficiency for Fenton-like reactions.<sup>15</sup> The effect of C<sub>H<sub>2</sub>O<sub>2</sub></sub> was studied by maintaining the rest of the parameters unchanged (*T* = 298 K, C<sub>MB</sub> = 100 mg L<sup>-1</sup>, ribbon dosage = 0.5 g L<sup>-1</sup> and pH = 3). Without H<sub>2</sub>O<sub>2</sub>, the C<sub>MB</sub> barely changes (Fig. 6(b)). It is well known that ZVI can directly react with organic molecules through the redox reaction, but there is

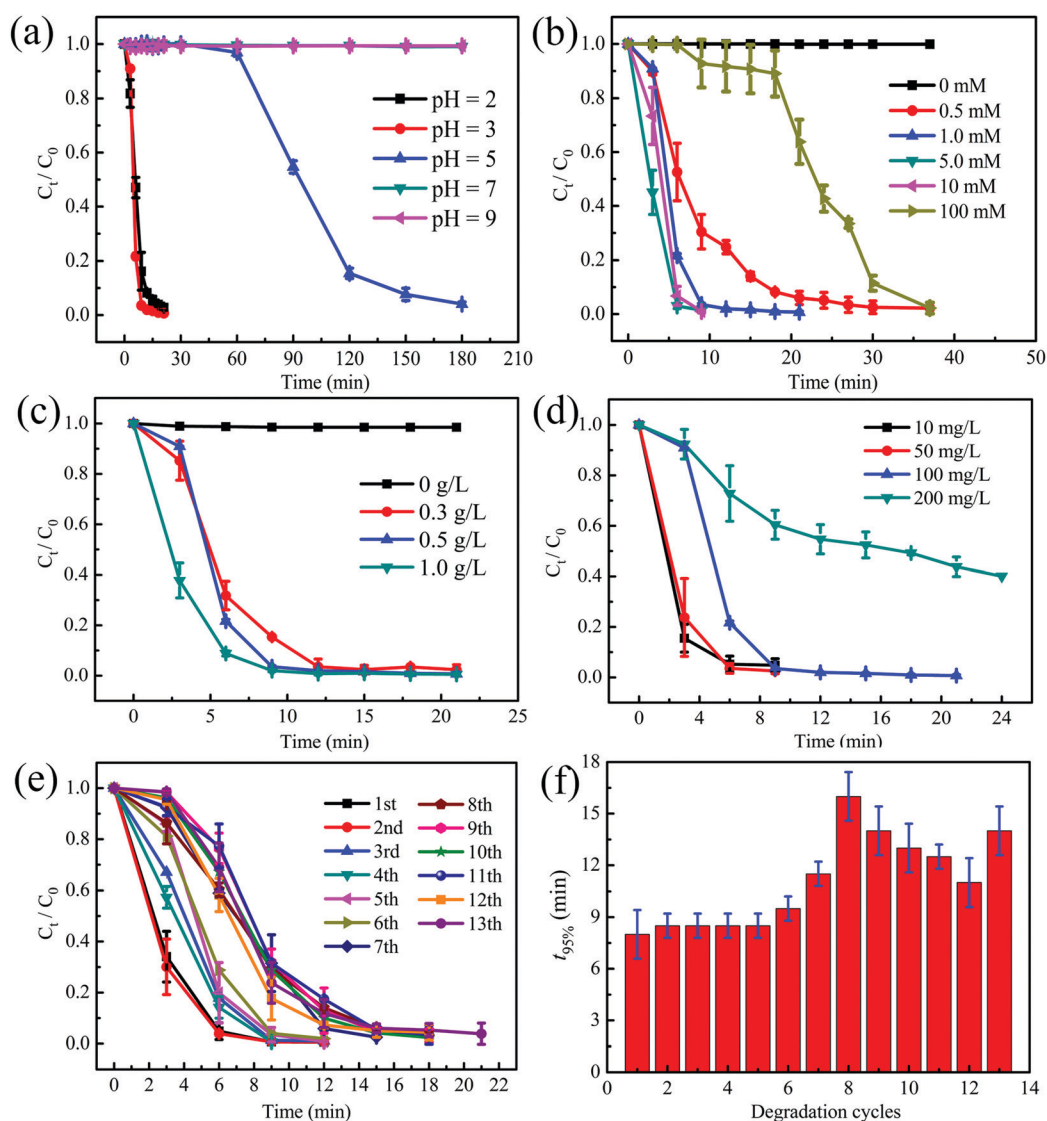
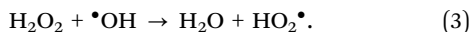


Fig. 6 Effects of (a) pH, (b) H<sub>2</sub>O<sub>2</sub> concentration, (c) ribbon dosage, and (d) dye concentration on MB degradation using the AQ Co<sub>4</sub> ribbons, (e) concentration change of the MB solution using the Co<sub>4</sub> amorphous ribbons from the 1st to 13th degradation cycles. (f) Time required for degrading 95% MB for each reaction cycle.

almost no degradation observed in our work for at least 38 minutes. This indicates that the reaction rate of ZVI directly degrading organic molecules is much lower than that through Fenton-like reactions. It is observed that appropriate addition of  $\text{H}_2\text{O}_2$  from 0.5 to 1.0, 5.0 and 10 mM can cause a rapid decrease in the reaction rate for the MB solution within the first 6 min, indicating that the reaction rate is sensitive to the  $\text{H}_2\text{O}_2$  concentration. Further increasing  $\text{H}_2\text{O}_2$  to 100 mM obviously hinders the reaction. When  $C_{\text{H}_2\text{O}_2}$  is too high, it can react with the  $\cdot\text{OH}$  through the following equation:<sup>33</sup>



As the strong oxidizing radicals  $\cdot\text{OH}$  are consumed by  $\text{H}_2\text{O}_2$  instead of organic molecules, the MB decomposition rate is decreased. So, the solution containing optimal  $C_{\text{H}_2\text{O}_2}$  is 0.5 to 10 mM at current reaction conditions.

The effect of the  $\text{Co}_4$  ribbon dosage during the MB degradation process was investigated by maintaining the other parameters unchanged ( $T = 298 \text{ K}$ ,  $C_{\text{MB}} = 100 \text{ mg L}^{-1}$ ,  $C_{\text{H}_2\text{O}_2} = 1 \text{ mM}$ , and  $\text{pH} = 3$ ), as shown in Fig. 6(c). Without the  $\text{Co}_4$  amorphous ribbon in the MB solution, no decomposition of MB is found within 21 minutes, suggesting that  $\text{H}_2\text{O}_2$  itself has little influence on the decrease of  $C_{\text{MB}}$  in 21 min with current reaction settings. As the amount of ribbons increases from 0.3 to  $1.0 \text{ g L}^{-1}$ , the reaction rate increases linearly. When using  $1.0 \text{ g L}^{-1}$  ribbons, the solution turns colourless after 6 min. A higher dosage of amorphous ribbons provides more active sites during the degradation process, which ensures the effective contact between the MB solution and amorphous ribbons and thus results in an obvious acceleration of the degradation process.

Fig. 6(d) shows the degradation efficiency dependence of  $C_{\text{MB}}$  with the other reaction parameters unchanged ( $T = 298 \text{ K}$ ,  $C_{\text{H}_2\text{O}_2} = 1 \text{ mM}$ , ribbon dosage =  $0.5 \text{ g L}^{-1}$  and  $\text{pH} = 3$ ). Obviously, it takes a longer time for degradations to finish with the increase of  $C_{\text{MB}}$ . When  $C_{\text{MB}}$  are 10, 50 and  $100 \text{ mg L}^{-1}$ , the degradation processes finish within 6, 6 and 9 min, respectively. While the  $C_{\text{MB}}$  is  $200 \text{ mg L}^{-1}$ , only 59% of MB is decomposed after 24 min. This is because once the  $C_{\text{MB}}$  reaches a certain large amount, the large organic molecules may adhere to the surface of the amorphous ribbons, preventing the adequate contact between  $\text{H}_2\text{O}_2$  and the surface of the ribbons, resulting in the low degradation efficiency.

Reusability of the  $\text{Co}_4$  amorphous ribbons were measured via cyclic degradation tests ( $T = 298 \text{ K}$ ,  $C_{\text{MB}} = 100 \text{ mg L}^{-1}$ ,  $C_{\text{H}_2\text{O}_2} = 1 \text{ mM}$ , ribbon dosage =  $0.5 \text{ g L}^{-1}$  and  $\text{pH} = 3$ ). The normalized concentration changes during the degradation process for each reaction cycle are presented in Fig. 6(e), and the time required to degrade 95% of the dye solution for all the cycles is summarized in Fig. 6(f). The  $\text{Co}_4$  amorphous ribbon shows good reusability as the MB can be completely decomposed within 15 min even after 13 reaction cycles. The reaction rates in the first 6 cycles are the same, with each cycle finishing in 9 min. From the seventh to thirteenth cycles, the degradation completion time varies between 12 and 15 min. The ribbons still show a high catalytic ability when the cyclic tests were

dropped after 13 experiments, indicating excellent reusability of the  $\text{Co}_4$  amorphous ribbons which is obviously better than that of the  $\text{Fe}_{78}\text{Si}_9\text{B}_{13}$  ribbons,<sup>19</sup> and this result is closely related to the surface morphologies of the reacted ribbons, which will be discussed below.

## Discussion

### Effect of Co addition on catalytic ability

Good degradation performance is closely related to the micro-structure of alloys.<sup>16,34</sup> According to the TEM images of AQ  $\text{Co}_0$  and  $\text{Co}_4$  in Fig. 1(b) and (c), respectively, the randomly oriented  $\alpha\text{-Fe}$  nanocrystals embedded in the amorphous matrix for the  $\text{Co}_0$  alloy, while the  $\text{Co}_4$  alloy shows the fully amorphous structure. It is well known that the amorphous structure is in a non-equilibrium state and energetically higher than the corresponding crystalline state.<sup>21</sup> In other words, amorphous alloys are chemically more active than their crystalline counterparts.<sup>35</sup> Therefore, ZVI in the FeCoPCCu amorphous ribbons can react more adequately with  $\text{H}_2\text{O}_2$  in the MB solution to produce strong oxidative radicals ( $\cdot\text{OH}$ ), which decomposes the organic dye molecules faster and finally shows a higher catalytic ability due to the improvement of the amorphous-forming ability by Co addition according to XRD and DSC. On the other hand, although Co does not directly supply electrons to participate in redox reactions due to the thermodynamics difference between  $\text{Co}^{2+}/\text{Co}$  and  $\text{Fe}^{2+}/\text{Fe}$ ,<sup>20</sup> Co contributes to the improvement of the decolorization ability of the FeCoPCCu alloys in another way. Previous research suggests that there is a chemical short-range order existing in the atomic structure of a melting state for an amorphous precursor, which can be characterized as the solute-centered atomic cluster in transition metal-metalloid amorphous alloys.<sup>36,37</sup> Like the P-centered antiprism-like and C-centered prism-like clusters in FePC amorphous alloys,<sup>38</sup> the addition of the Co element may also lead to special P/C-centered atomic clusters. As the heats of mixing of Fe-P, Fe-C, Co-P and Co-C bonds are negative, being  $-39.5$ ,  $-50$ ,  $-35.5$  and  $-42 \text{ kJ mol}^{-1}$ , respectively,<sup>20</sup> the micro-alloying provides a large number of Fe-P, Fe-C, Co-P and Co-C bonds. This enables the formation of more local galvanic couples, which accelerate the transfer of electrons in ZVI and further improve the catalytic performance of the alloy. This result is similar to previous works.<sup>18,19,21</sup> Besides, the nano-whisker and micro-crack structures formed during degradation using the  $\text{Co}_4$  amorphous ribbons have been proved to be characteristic for an efficient catalyst in Fenton-like reactions.<sup>33</sup>

As a result, appropriate addition of Co is effective in promoting the catalytic decolorization of FePCCu alloys.

For the  $\text{Co}_{10}$  alloy, the relatively weak degradation ability is closely related to the stable oxidized film formed on the surface of the ribbons as illustrated by the surface morphology and corrosion behavior analyses. The formation of oxidized layer on the ribbon can effectively separate the inner metal atoms from the MB solution, becoming the main barrier in the electron transfer between ZVI and the dye solution.<sup>39</sup> Meanwhile, the

total number of Fe atoms in the alloys will be reduced due to the excessive Co substitution. According to the Fenton-like reactions,<sup>33</sup> ZVI is an essential participant during the Fenton-like reactions; thus, the decreased number of Fe atoms also hinders the degradation process. As a result, the Co<sub>10</sub> amorphous ribbons show a low catalytic performance in the Fenton-like reactions in this work.

### Reusability

To understand the reason for excellent reusability of the Co<sub>4</sub> ribbons, surface morphologies and elemental compositions of the reacted Co<sub>4</sub> ribbons after the 12th cycle were analyzed, as shown in Fig. 7. Nano-whisker and micro-crack structures are observed all over the ribbon surface (Fig. 7(a)), providing continuous electron transfer channels from the surface of the reacted ribbon during the cyclic tests. The enlarged image of Fig. 7(a) is shown in Fig. 7(b), which reveals details of the reaction process. A lamellar product layer shedding from the ribbon surface is clearly found. To analyze the elemental difference between the underlying matrix and product layer, EDS was performed on the representative regions (red cross and yellow cross) with results shown in Fig. 7(c) and (d) respectively. The changes of element contents, including Fe, Co, P, C and Cu elements, are clearly observed. Because there is not much content change in the Co and Cu elements (see Table 2), only the Fe, P and O contents are given here on the EDS maps. As the elemental contents of Fe and P approximate the nominal composition of the Co<sub>4</sub> alloy (Fig. 7(c)), the red cross

region is a “fresh” Co<sub>4</sub> ribbon surface underneath. In contrast, the O content in the product layer is much higher than that in the matrix, indicating the formation of an oxide layer. The Fe content reduces obviously after the reaction as Fe is involved in Fenton-like reactions. The increase of P in the product layer may be related to the produced iron phosphates on the surface during the degradation. The reacted top layer (nano-whiskers) continuously falls off, which allows the underneath “fresh” surface to provide Fe<sup>0</sup> for the Fenton-like reactions. This explains the excellent reusability of the Co<sub>4</sub> amorphous ribbons.

### Reaction process using FeCoPCCu ribbons

Based on the above analyses, the degradation process of the Co<sub>4</sub> amorphous ribbons in the MB solution can be summarized. ZVI on the surface of ribbon is an indispensable source for Fenton-like reactions, which reacts with H<sub>2</sub>O<sub>2</sub> to produce a large number of strongly oxidative •OH groups. The produced •OH can fully contact with dye molecules in the solution with mechanical stirring, resulting in the cleavage of dye bonds. Thus, the large MB molecules are decomposed into small molecules including CO<sub>2</sub>, H<sub>2</sub>O, NO<sup>3-</sup>, SO<sub>4</sub><sup>2-</sup>, etc.<sup>19</sup> With minor Co addition, the well-developed nano-whisker and micro-crack structures can be formed, allowing the MB solution to penetrate further into the ribbon below the oxide layer. Meanwhile, the local galvanic couple structures formed between the Fe–C, Co–C, Fe–P and Co–P bonds in the FeCoPCCu amorphous ribbon accelerate the electron transfer from ZVI to the solution.

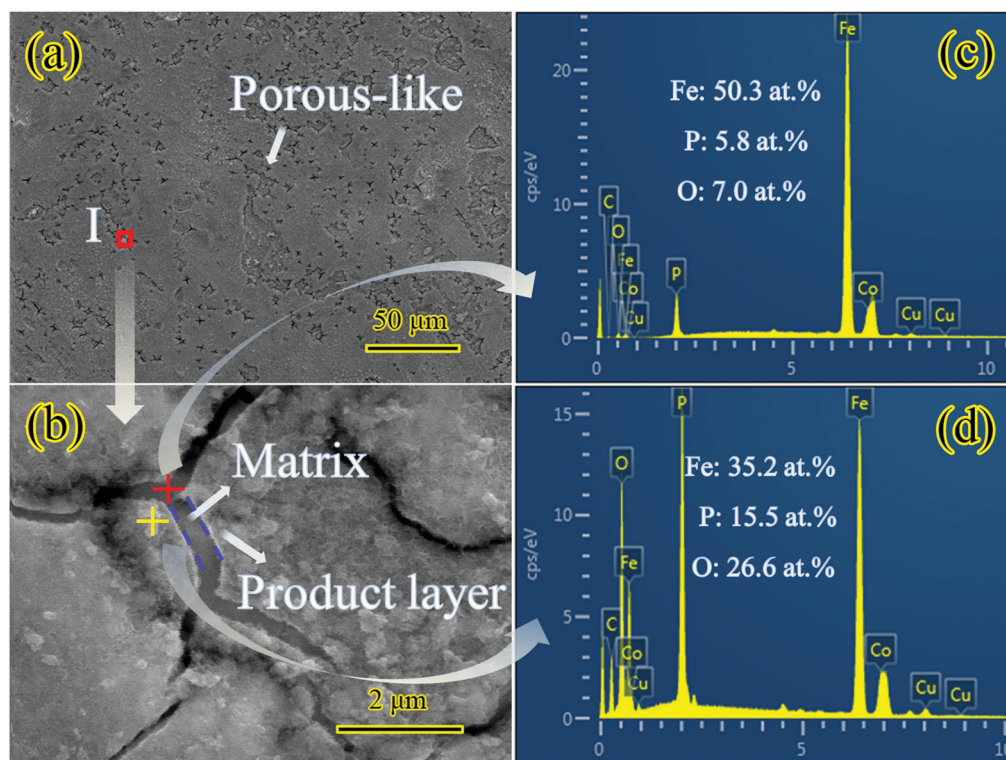


Fig. 7 (a) SEM micrographs of the reacted Co<sub>4</sub> amorphous ribbon after 12 degradation cycles in the MB solution; (b) enlarged image of (a); (c) and (d) EDS analysis corresponding to the underlying matrix (red cross) and product layer (yellow cross) in (b), respectively.



Thus, the Co<sub>4</sub> amorphous ribbon shows a high catalytic ability during the degradation process.

## Conclusion

In summary, the effects of Co addition on the decolorization performance of FePCCu ribbons were explored in this paper. It was found that Co addition can result in a fully amorphous structure of alloys, which is beneficial to the degradation of the MB solution. Different Co contents have different degradation abilities in the MB solution. The crystalline structure of a Co-free alloy leads to a relatively low catalytic performance. The alloy with 4 at% Co addition exhibits the highest catalytic degradation ability, which is closely related to the unique amorphous structure, nano-whisker and micro-crack structures formed during the decolorization process and local galvanic couples between strong Fe–C, Co–C, Fe–P and Co–P bonds. With excessive Co addition (10 at%), the oxidized layer formed on the reacted surface of ribbons reduces their degradation ability in the MB solution, which is confirmed by the good corrosion resistance of the alloy. Moreover, the Fe<sub>79.2</sub>Co<sub>4</sub>P<sub>10</sub>C<sub>6</sub>Cu<sub>0.8</sub> ribbon exhibits good reusability due to the continuous shedding of the nano-whisker oxidation layer. Our work reveals the highly efficient catalytic ability of a novel FeCoPCCu alloy in Fenton-like reactions, and this alloy is proposed as a new catalyst for sewage treatment.

## Conflicts of interest

There are no conflicts of interest to declare.

## Acknowledgements

This work was supported by the National Natural Science Foundation of China (Grant No. 51631003, 51401052, and 51871237) and the National Key Research and Development Program of China (Grant No. 2016YFB0300502).

## References

- 1 C. Noubactep, *Water Sanit.*, 2010, **4738**, 663–670.
- 2 F. L. Fu, D. D. Dionysiou and L. Hong, *J. Hazard. Mater.*, 2014, **267**, 194–205.
- 3 Z. K. Xiong, B. Lai and P. Yang, *Chemosphere*, 2018, **194**, 189–199.
- 4 C. B. Wang and W. X. Zhang, *Environ. Sci. Technol.*, 1997, **31**, 2154–2156.
- 5 W. X. Zhang, *J. Nanopart. Res.*, 2003, **5**, 323–332.
- 6 H. J. Zhu, Y. F. Jia, W. Xing and W. He, *J. Hazard. Mater.*, 2009, **172**, 1591–1596.
- 7 L. Yang, L. Lv, S. J. Zhang, B. C. Pan and W. M. Zhang, *Chem. Eng. J.*, 2011, **178**, 161–167.
- 8 F. Scaglione and L. Battezzati, *J. Mater. Sci.*, 2015, **50**, 5238–5243.
- 9 A. Inoue and B. L. Shen, *J. Mater. Res.*, 2003, **18**, 2799–2806.
- 10 A. Inoue, B. L. Shen and C. T. Chang, *Acta Mater.*, 2004, **52**, 4093–4099.
- 11 Z. P. Lu, C. T. Liu, J. R. Thompson and W. D. Porter, *Phys. Rev. Lett.*, 2004, **92**, 245503.
- 12 B. An, Y. J. Li, Y. Liu, Y. G. Wang, L. C. Zhang and W. M. Wang, *J. Alloys Compd.*, 2014, **593**, 16–23.
- 13 A. L. Greer, *Science*, 1995, **267**, 1947–1953.
- 14 Y. Tang, Y. Shao, N. Chen and K. F. Yao, *RSC Adv.*, 2015, **5**, 6215–6221.
- 15 X. F. Wang, Y. Pan, Z. R. Zhu and J. L. Wu, *Chemosphere*, 2014, **117**, 638–643.
- 16 Y. Tang, Y. Shao, N. Chen, X. Liu, S. Q. Chen and K. F. Yao, *RSC Adv.*, 2015, **5**, 34032.
- 17 J. Q. Wang, Y. H. Liu, M. W. Chen, G. Q. Xie, D. V. Louzguine-Luzgin, A. Inoue and J. H. Perepezko, *Adv. Funct. Mater.*, 2012, **22**, 2567–2570.
- 18 S. H. Xie, P. Huang, J. J. Kruzic, X. R. Zeng and H. X. Qian, *Sci. Rep.*, 2016, **6**, 21947.
- 19 Q. Q. Wang, M. X. Chen, P. H. Lin, Z. Q. Qiang, C. L. Chu and B. L. Shen, *J. Mater. Chem. A*, 2018, **6**, 10686.
- 20 A. Takeuchi and A. Inoue, *Mater. Trans.*, 2005, **46**, 2817–2829.
- 21 X. D. Qin, Z. W. Zhu, G. Liu, H. M. Fu, Z. H. Wang, A. M. Wang, H. Li and H. F. Zhang, *Sci. Rep.*, 2015, **5**, 18226.
- 22 C. Q. Zhang, Q. Sun and K. Liu, *J. Alloys Compd.*, 2018, **741**, 1040–1047.
- 23 Z. G. Shi, R. Li and T. Zhang, *J. Alloys Compd.*, 2019, **778**, 302–308.
- 24 Y. L. Jin, X. D. Fan, M. He, X. C. Liu and B. L. Shen, *Sci. China: Technol. Sci.*, 2012, **55**, 3419–3424.
- 25 Z. Jia, J. Kang, W. C. Zhang, W. M. Wang, C. Yang, H. Sun, D. Habibi and L. C. Zhang, *Appl. Catal., B*, 2017, **204**, 537–547.
- 26 S. Nam and P. G. Tratnyek, *Water Res.*, 2000, **34**, 1837–1845.
- 27 S. X. Liang, Z. Jia, W. C. Zhang, W. M. Wang and L. C. Zhang, *Mater. Des.*, 2017, **119**, 244–253.
- 28 S. Q. Chen, Y. Shao, M. T. Cheng and K. F. Yao, *J. Non-Cryst. Solids*, 2017, **473**, 74–78.
- 29 S. Khalid and C. B. Cao, *New J. Chem.*, 2017, **41**, 5794–5801.
- 30 A. Pardo, M. C. Merino, E. Otero, M. D. López and A. M. Hich, *J. Non-Cryst. Solids*, 2006, **352**, 3179–3190.
- 31 D. D. Xu, B. L. Zhou, Q. Q. Wang, J. Zhou, W. M. Yang, C. C. Yuan, L. Xue, X. D. Fan, L. Q. Ma and B. L. Shen, *Corros. Sci.*, 2018, **138**, 20–27.
- 32 Z. H. Dan, F. X. Qin, Y. Zhang, A. Makino, H. Chang and N. Hara, *Mater. Charact.*, 2016, **121**, 9–16.
- 33 S. S. Lin and M. D. Gurol, *Environ. Sci. Technol.*, 1998, **32**, 1417–1423.
- 34 S. Q. Chen, G. N. Yang, S. T. Luo, S. J. Yin, J. L. Jia, Z. Li, S. H. Gao, S. Yang and K. F. Yao, *J. Mater. Chem. A*, 2017, **5**, 14230.
- 35 C. Q. Zhang, Z. Wang, H. F. Zhang and Q. Zhuang, *Sci. Bull.*, 2011, **56**, 3988–3992.
- 36 D. B. Miracle, *Acta Mater.*, 2006, **54**, 4317–4336.
- 37 S. Y. Meng, H. B. Ling, Q. Li and J. J. Zhang, *Scr. Mater.*, 2014, **81**, 24–27.
- 38 S. X. Zhou, B. S. Dong, J. Y. Qin, D. R. Li, S. P. Pan, X. F. Bian and Z. B. Li, *J. Appl. Phys.*, 2012, **112**, 023514.
- 39 C. Q. Zhang, Z. W. Zhu and H. F. Zhang, *J. Phys. Chem. Solids*, 2017, **110**, 152–160.